Supporting Information

Polyoxometalate-Mediated Confined Self-Assembly of Sandwich-Structured Mesoporous Polymer@rGO for High-Performance Aqueous Zinc-Iodine Batteries

Wenyang Lu,[†a] Lebing Liu, [†a] Weibo Gong,[†b] Hengyue Xu,[c] FengYang Xie,[a] Xingrui Ji,[a] Tingting Zhang,[d] Shaohua Liu,[d] Facai Wei*[a] Chunxian Guo*[a]

a. Institute of Materials Science and Devices, School of Materials Science and Engineering, Suzhou University of Science and Technology, Suzhou 215009, China. E-mail: cxguo@usts.edu.cn

b. Suzhou Laboratory, Suzhou, 215100 China

c. Institute of Biopharmaceutical and Health Engineering, Tsinghua Shenzhen International Graduate School, Tsinghua University, Shenzhen, 518055 P. R. China

d. State Key Laboratory of Precision Spectroscopy, Engineering Research Center of Nanophotonics & Advanced Instrument (Ministry of Education), School of Physics and Electronic Science, East China Normal University, Shanghai, 200241 P. R. China

Experimental Section

Chemicals and Materials

1,5-Diaminonaphthalene (1,5-DAN, 99%, RG), ammonium molybdate tetrahydrate ($(NH_4)_6Mo_7O_{24}\cdot 4H_2O$, AMT, 99%, RG), 1,3,5-trimethylbenzene (TMB), zinc trifluoromethanesulfonate ($Zn(CF_3SO_3)_2$), and iodine (I_2, 99%) were purchased from Adamas Reagent Co., Ltd. Triblock copolymer Pluronic F127 ($PEO_{106}PPO_{70}PEO_{106}$, M_n = 12,600 g mol^{-1}), polyvinylidene fluoride (PVDF), and N-methyl-2-pyrrolidone (NMP) were obtained from Sigma-Aldrich. Ammonium persulfate (APS) was supplied by Macklin Reagent Co., Ltd. Ethanol (99.7%, AR) was purchased from General-reagent®. Graphene oxide (GO) was acquired from Nanjing XFNANO Materials Tech Co., Ltd. All chemicals were used as received without further purification. Deionized water (18.2 MΩ·cm) was prepared using a Millipore Direct-Q purification system.

Characterization Methods

Scanning electron microscopy (SEM) images were acquired using a Zeiss Gemini 450 instrument. Transmission electron microscopy (TEM) was performed on a JEM-2100F microscope equipped with a 200 kV field emission gun. Samples for TEM analysis were prepared by drop-casting diluted dispersions onto carbon-coated copper grids (200 mesh) followed by drying at room temperature for 20 minutes. X-ray diffraction (XRD) patterns were collected on an Empyrean diffractometer (Cu Kα radiation, $\lambda = 1.54056$ Å, 40 kV, 40 mA) with a scanning range of 5°–80° and a rate of 10° min^{-1}. Fourier-transform infrared (FT-IR) spectra were recorded on a Nicolet iS50 spectrometer (Thermo Fisher) in the range of 4000–500 cm^{-1}. Nitrogen adsorption-desorption isotherms were measured using a Quantachrome Quadrasorb SI analyzer at 77 K. Prior to measurements, samples were degassed at 120 °C for 12 hours. Specific surface areas were calculated via the Brunauer-Emmett-Teller (BET) method, and pore size distributions were derived using the Barrett-Joyner-Halenda (BJH) model.

Material Synthesis

Preparation of Mo-mPDAN@rGO Nanosheets

In a typical synthesis, 100 mg of F127 was dissolved in 7 mL of a mixed solvent (4 mL deionized water + 3 mL ethanol) in a 20 mL glass vial under stirring. Subsequently, 200 μL of TMB was added, and the mixture was stirred for >1 h to form micellar aggregates. A 0.2 mL GO dispersion (~2 mg mL^{-1}, synthesized via modified Hummers' method) was introduced and stirred for 30 minutes. A solution of 12.5 mg 1,5-DAN in 1 mL 0.1 M HCl was added dropwise, followed by 30 minutes of continuous stirring. After adding 1 mL of AMT solution (1.2 M in H_2O) and 500 μL of APS solution (1 M in H_2O), the polymerization of 1,5-DAN was initiated. The reaction proceeded for 8 h before the product was collected via centrifugation. The precipitate was redispersed in 20 mL deionized water, transferred to a Teflon-lined autoclave, and subjected to hydrothermal treatment at 180 °C for 12 h. The final product (Mo-mPDAN@rGO) was obtained by repeated centrifugation-washing cycles with deionized water and ethanol, followed by vacuum drying at 60 °C. Non-porous Mo-PDAN@rGO was synthesized using the same protocol but omitting F127 and TMB. Reduced graphene oxide (rGO) was prepared via identical hydrothermal treatment of the parent GO dispersion.

Preparation of I_2-Loaded Composites (I_2/Mo-mPDAN@rGO, I_2/rGO)

For iodine loading, 400 mg of I_2 and 50 mg of the host material were placed in a 10 mL glass vial within a sealed reactor. The reactor was heated at 120 °C for 12 h to facilitate iodine sublimation-diffusion. The iodine content in the composite was determined by mass difference before and after loading.

Electrochemical Measurements

Electrodes were prepared by mixing the iodine-loaded active material, PVDF binder, and Super P carbon black in a 7:2:1 weight ratio. The slurry was ground with NMP to form a homogeneous paste, which was then coated onto carbon cloth (12 mm diameter) and dried at 60 °C for 12 h. The active mass loading ranged from 0.7 to 1.5 mg cm^{-2}. CR2032 coin cells were assembled in an Ar-filled glovebox using a zinc foil anode, glass fiber separator (Whatman® GF/C), and 0.5 M $Zn(CF_3SO_3)_2$ aqueous electrolyte. Cyclic voltammetry (CV) and electrochemical impedance spectroscopy (EIS) were performed using a CHI760E electrochemical workstation. EIS measurements were conducted at a frequency range of 0.01 Hz–100 kHz with an AC amplitude of 5 mV. Galvanostatic charge-discharge tests were carried out on a LAND CT2001A battery tester within a voltage window of 0.5–1.6 V (vs. Zn/Zn^{2+}). All specific capacities and current densities were normalized to the mass of iodine.

Computational details

All DFT calculations for periodic material systems were performed with the Vienna Ab initio simulation package (VASP)[1] using the projector-augmented wave (PAW) method.[2] The exchange–correlation function was handled using the generalized gradient approximation (GGA) formulated by the Perdew-Burke-Ernzerhof (PBE).[3] The van der Waals (vdW) interactions are described with the DFT-D3 method in Grimme's scheme.[4,5] The interaction between the atomic core and electrons was described by the projector augmented wave method. The plane-wave basis set energy cutoff was set to 500 eV.[6] The Brillouin zone was sampled with a 1 × 1 × 1 grid centered at the gamma (Γ) point for geometry relaxation. All the slabbed models possessed a vacuum spacing of ≈15 A˚ sampled, ensuring negligible lateral interaction of adsorbates.[7] The bottom layers about half of the structure were kept frozen at the lattice position.[8] All structures with a dynamic magnetic moment were fully relaxed to optimize without any restriction until their total energies were converged to $< 2\times10^{-5}$ eV,[9,10] and the average residual forces were < 0.05 eV/Å.[11,12]

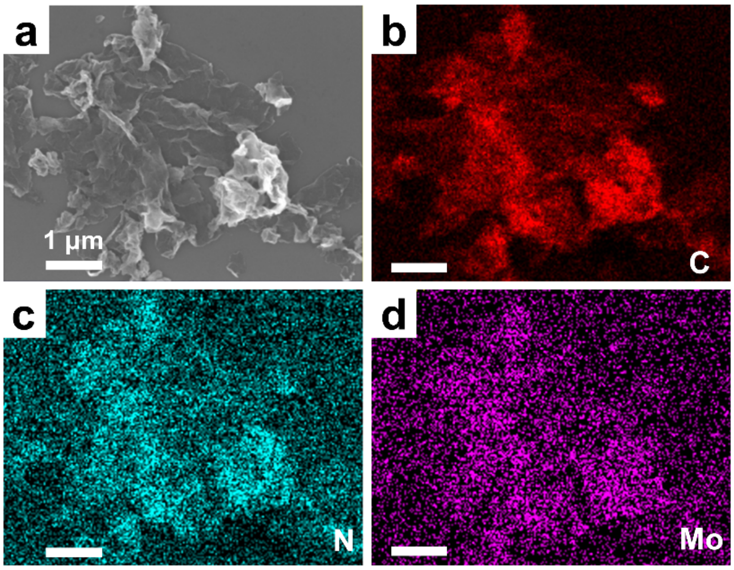

Fig. S1 The EDX element mapping image of Mo-mPDAN@rGO sample.

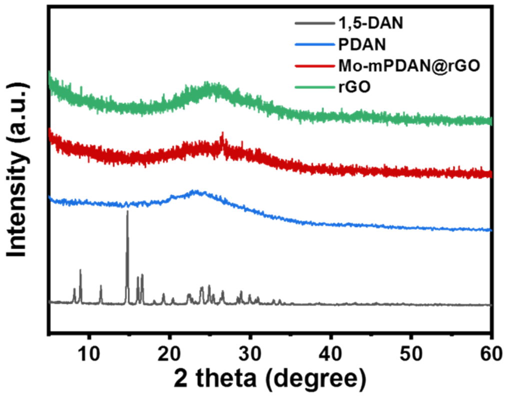

Fig. S2 The XRD pattern of different samples.

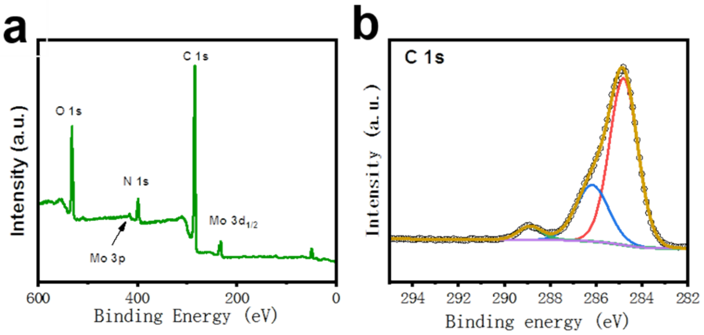

Fig. S3 (a) XPS full spectrum, (b) C 1s fine spectrum of Mo-mPDAN@rGO.

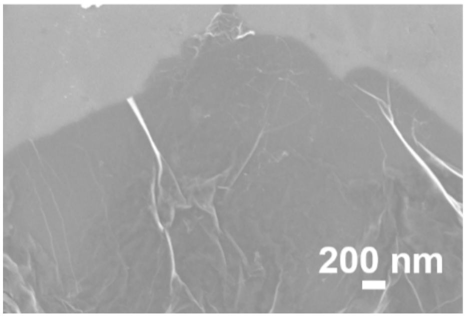

Fig. S4 The SEM image of the product obtained without adding F127.

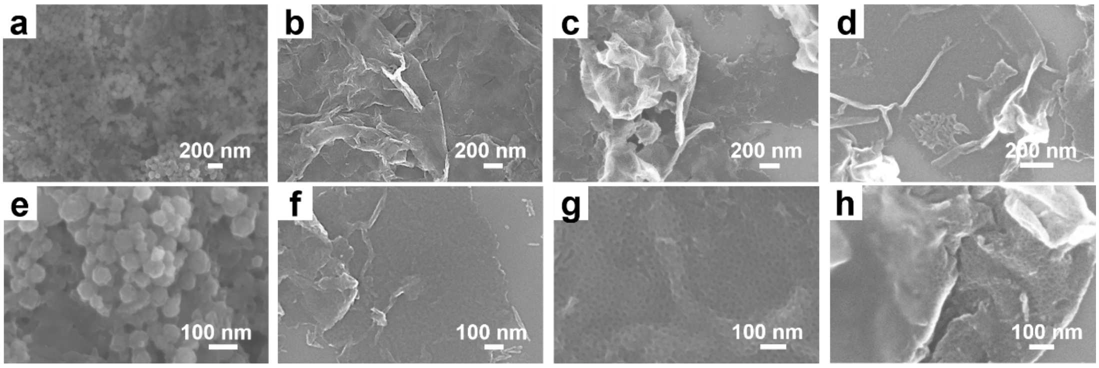

Fig S5 SEM images of the products obtained by changing the dosage of GO: (a, e) 0 µL; (b, f) 50 µL; (c, g) 200 µL; (d, h) 400 µL.

The quantity of GO exerted a critical influence on the morphological evolution of the hybrid nanosheets. As demonstrated in Figure S3a and S3e, the complete omission of GO from the synthesis system resulted in the formation of irregular granular aggregates lacking discernible mesoporosity. Upon introduction of GO (200 µL), the granular morphology disappeared completely, and a hierarchical mesoporous architecture emerged (Fig S5b, S5f). Notably, the optimized GO concentration (200 µL) enabled the formation of uniformly structured mesoporous nanosheets with lateral dimensions exceeding several micrometers (Fig S5c, S5g). However, excessive GO addition (e.g., 400 µL) disrupted the self-assembly process, yielding nanosheets with heterogeneous mesopore distribution characterized by regions of sparse mesoporosity interspersed with non-porous domains (Fig S5d, S5h). These observations collectively underscore the dual role of GO as both a 2D structural director and a confinement substrate, which is essential for the formation of sandwich-like nanosheet morphology with mesoporosity. The template effect of GO likely arises from π–π stacking interactions between the aromatic domains of GO and the growing polymer chains, coupled with electrostatic guidance of POM-bridged micelle alignment.

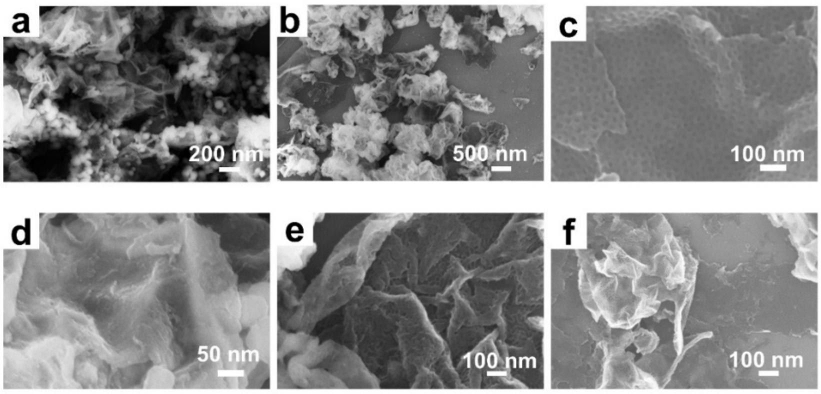

Fig.S6 SEM images of the products obtained by changing the dosage of TMB: (a, d) 0 μL, (b, e) 100 μL, (c, f) 200 μL.

TMB also plays a critical role in mesopore formation. When TMB is excluded from the system, as shown in Figure S6a and S6d, spherical particles emerge alongside similar non-porous nanosheet morphologies. This phenomenon likely arises because TMB modulates the hydrophilic-hydrophobic balance of micelles, stabilizing them to guide mesopore formation. Without TMB, unstable micelles fail to direct mesostructure development, while excess F127 acts as a surfactant to form uniform spherical aggregates by altering surface tension. When TMB concentration increases to 100 μL, sparse mesopores appear on the 2D nanosheet surfaces (Figures S6b, S6e). Further increasing TMB to 200 μL yields homogeneous 2D mesoporous sheets with slightly enlarged pore diameters (Figures S6c, S6f). These results indicate that trace hydrophobic TMB acts as a swelling agent in this system, modulating mesopore dimensions through micelle size regulation.

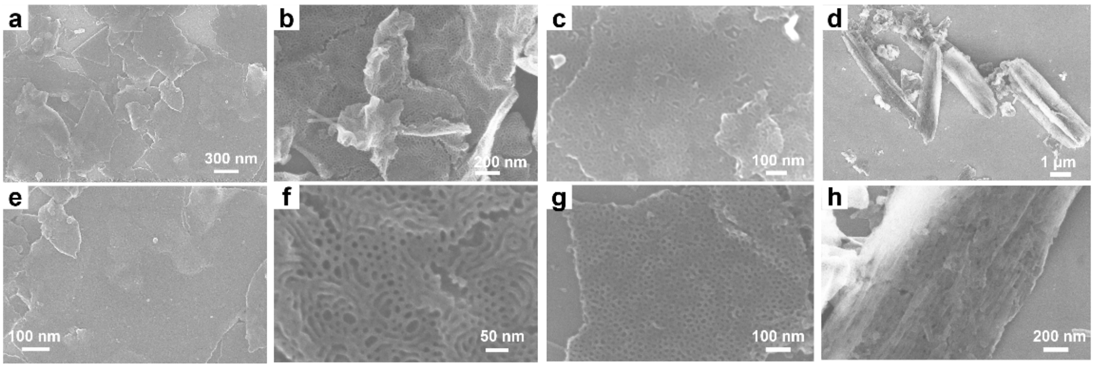

Fig.S7 SEM images of the products obtained by changing the molar ratio of AMT/1, 5-DAN: (a, e) 0; (b, f) 0.05; (c, g) 0.26; (d, h) 0.4.

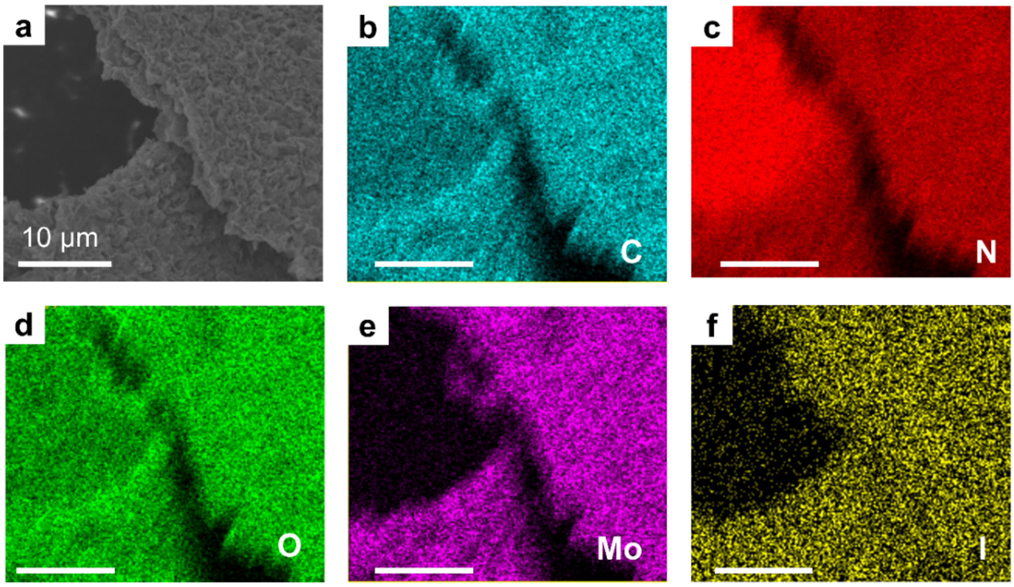

Fig. S8 The EDX images of I_2/Mo-mPDAN@rGO.

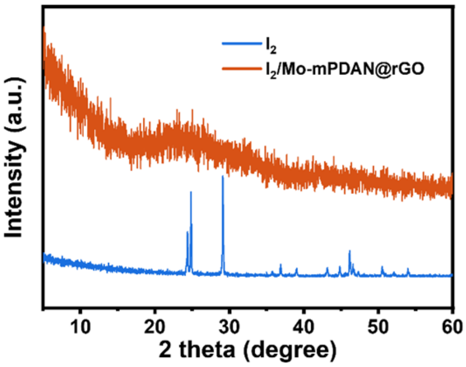

Fig S9 XRD patterns of I_2 and I_2/Mo-mPDAN@rGO.

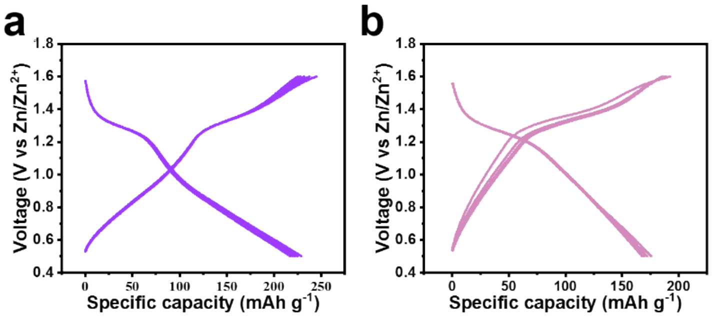

Fig 10. (a) GCD curves of I_2/Mo-mPDAN@rGO and (b) I_2/rGO electrodes for the first five cycles at a current density of 0.2A g^{-1}.

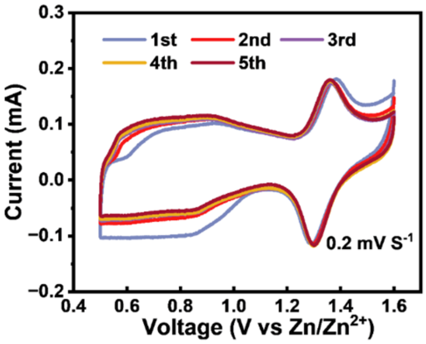

Fig.11 CV curves of the first 5 cycles of I_2/Mo-mPDAN@rGO cathode at a sweep rate of 0.2 mV s^{-1}.

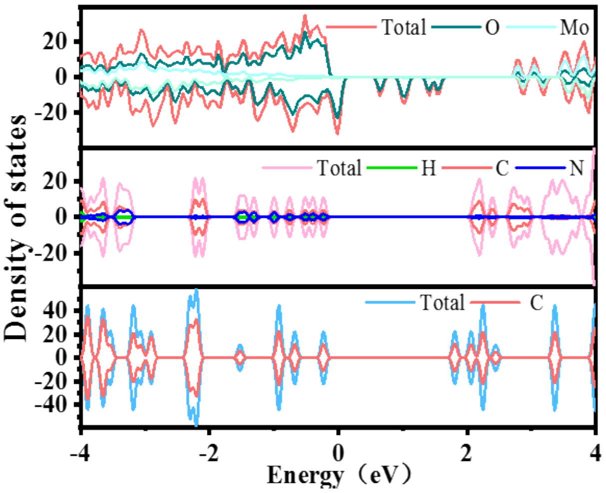

Fig 12. Total and partial density of states for AMT (top), PDAN (middle), and rGO (bottom).

References

(1) Kresse, G.; Furthmüller, J. Comput. Mater. Sci. 1996, **6** (1), 15.

(2) Blöchl, P. E. Projector Augmented-Wave Method. Phys. Rev. B 1994, **50** (24), 17953.

(3) Ernzerhof, M.; Scuseria, G. E. J. Chem. Phys. 1999, **110** (11), 5029.

(4) Grimme, S.; Antony, J.; Ehrlich, S.; Krieg, H. J. Chem. Phys. 2010, **132** (15), 154104.

(5) Guan, D.; Xu, H.; Zhang, Q.; Huang, Y. C.; Shi, C.; Chang, Y. C.; Xu, X.; Tang, J.; Gu, Y.; Pao, C. W.et al. Adv. Mater. 2023, **35**, 2305074.

(6) Xu, H.; Zhang, F.; Fang, L.; Xu, Y.; Yu, Z.-W.; Ma, L.; Guan, D.; Shao, Z. Inorg. Chem. 2024, **63** (42), 19570.

(7) Xiao, W.; Yoo, K.; Kim, J. H.; Xu, H. Adv. Sci. 2023, 2303916.

(8) Xiao, W.; Kiran, G. K.; Yoo, K.; Kim, J. H.; Xu, H. Small 2023, **19** (20), 2206750.

(9) Xu, H.; Zhu, J. Z.; Zou, C.; Zhang, F.; Ming, D.; Guan, D.; Ma, L. Energy Fuels 2023, **37** (21), 16781.

(10) Zheng, Q.; Xu, H.; Yao, Y.; Dai, J.; Wang, J.; Hou, W.; Zhao, L.; Zou, X.; Zhan, G.; Wang, R.et al.. Angew. Chem. Int. Ed. 2024, **63** (19), e202401386.

(11) Xu, H. Chem. Phys. Lett. 2024, **851**, 141492.

(12) Xiao, W.; Yoo, K.; Kim, J.; Xu, H. ACS Nano 2024, **18** (47), 32732.